Journal of Computational Physics **166,** 271–301 (2001)
doi:10.1006/jcph.2000.6652, available online at http://www.idealibrary.com on IDEAL®

Numerical Instabilities in Upwind Methods: Analysis and Cures for the "Carbuncle" Phenomenon

Maurizio Pandolfi* and Domenic D'Ambrosio†,[1]

**Dipartimento di Ingegneria Aeronautica e Spaziale, Politecnico di Torino, Corso Duca degli Abruzzi, 24, 10129 Torino, Italy; and †Aerodynamisches Institut, RWTH Aachen, Wuellnerstr. zw. 5 u. 7, 52064 Aachen, Germany*
E-mail: pandolfi@polito.it; domenic@athena.polito.it

Received March 22, 1999; revised April 13, 2000

Some upwind formulations promote severe instabilities that originate in the numerical capturing of shocks; this is known as the "carbuncle" phenomenon. An analysis of the linearized form of the algorithms is carried out to explain and predict the generation of such instabilities. The information obtained is then used to design remedies that only slightly and locally modify the original schemes.

Key Words: fluid dynamics; shock waves; upwind methods; numerical instability; "carbuncle" phenomenon.

CONTENTS

1. *Introduction.*
2. *The carbuncle phenomenon.*
3. *Upwind methods.*
4. *Two significant examples.*
5. *Analyses of the linearized algorithms.*
6. *Cures for the carbuncle.*
7. *Conclusions.*

1. INTRODUCTION

Strong shock waves and density or shear layers characterize high-speed flows. These features affect the choice of the most appropriate numerical methods to be used. In particular, the requirement of capturing numerically strong shock waves moves attention toward upwind methods. Among these, the *flux difference splitting* (FDS) approach looks to be the

[1] Financed by the European Commission with a TMR Marie Curie Research Training Grant.

0021-9991/01 $35.00

most promising, since it combines good shock-capturing properties with the capability of correctly dealing with density or shear layers, introducing, in the latter case, only a small amount of artificial diffusion into the solution (in the cases of steady density or shear layers aligned with the grid, no artificial diffusion is injected). Unfortunately, several numerical experiments based on FDS methods have given unacceptable results, even for the simplest problems: the structure of numerically captured shock waves often becomes widely distorted and the resulting picture would seem to justify the nickname of *carbuncle* that is found in literature. A very clear introduction on this subject and some preliminary suggestions on how to circumvent shortcomings are given in [17]; some numerical experiences on the problem have previously been reported in the literature, though not in detail.

In this paper we would like to contribute to the understanding of such a disturbing deficiency and to suggest remedies to resolve the problem.

First, we start with an analysis of some significant aspects of the carbuncle numerical phenomenon. Then, we review some of the most popular upwind methods to predict compressible flows. Afterwards, we show the results of numerical experiments that were obtained in two significant examples proposed in [17]. These clearly show the carbuncle instability and may represent the basis for understanding where the problem arises and for discussing possible remedies. At this point, we develop some simple analyses to learn how the different methods behave in the presence of perturbations that may trigger the instability process. Finally, we look at some suggestions that have been reported in the literature to prevent such a disturbing numerical deficiency and we then propose a cure.

2. THE CARBUNCLE PHENOMENON

The numerical instability that, in some cases, afflicts the numerical capturing of shock waves is defined as the "carbuncle phenomenon." A typical result of this kind of disturbing event is shown in Fig. 1 and concerns the numerical simulation of a $M_\infty = 20$ inviscid flow around a circular cylinder, a problem which is today considered a normal routine in

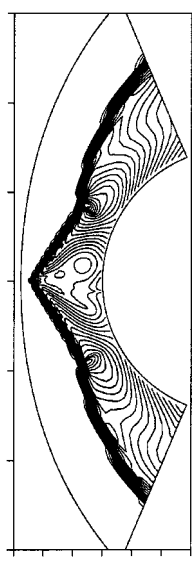

FIG. 1. Carbuncle in the supersonic inviscid flow around a blunt body at $M_\infty = 20$ (density contours).

computational fluid dynamics. The distorted shape of the shock is not due to a programming bug: the code used, which adopts a flux-difference splitting method (which in the following is indicated as FDSPAN), works correctly for other problems and did not show any disturbances of this kind before the numerical grid was refined in the circumferential direction beyond a certain extent.

The carbuncle phenomenon does not only belong to the numerical simulation of supersonic flows on blunt bodies; it can, for instance, also be found in other problems, such as in the numerical capturing of quasi-conical shock waves around slender bodies [10] or in the numerical simulation of interstellar flows in astrophysics [27]. Nevertheless, since our experience of the problem commenced when we were dealing with blunt bodies, we decided to start from this point to illustrate some plain facts that we noticed during our study.

From numerical experiments on computing the classical supersonic flow around a blunt body, the following was observed:

a. The carbuncle phenomenon originates inside the narrow computational region where a normal shock (in which the upstream relative flow is perpendicular to the shock front) is numerically captured, but only when it is well aligned with one family of grid coordinates; weak disturbancies, even at the round-off error level, in the initially regular structure of the captured shock may induce severe instabilities that badly degenerate into large oscillations, both in space and in time. If the numerical capturing of the shock is replaced by its explicit treatment, the *shock-fitting technique* (SHOFIT), all generations of the carbuncle instability are prevented, since the shock-capturing region is absent.

b. The grid aspect ratio is very significant in the establishment of the carbuncle phenomenon: very elongated grid elements along the normal to the shock promote instabilities, whereas meshes stretched along the tangent to the shock have a damping effect; this point is clearly visible in Fig. 2, where the blunt-body test case has been computed using different grids, which have the same number of points (20) in the radial direction, but a different number of points (20, 80, 160, and 320) in the tangential direction.

c. The carbuncle phenomenon occurs in those upwind methods that solve the Riemann problem (RP), defined at the interface between two adjacent cells, on the basis of a three-wave model.

d. Carbuncle-ike features are more evident in the plain first-order integration scheme, than in more accurate reconstruction schemes, which denote a less severe development of instabilities; this statement is supported by the numerical results shown in Fig. 3, where first-and second-order results obtained using the same grid are compared.

e. The carbuncle represents a numerical instability that is closely related to the convective terms of the equations (the Euler part), which govern compressible flows; the effect of the diffusive terms which are present in the Navier–Stokes equations is not sufficient to improve the (poor) quality of the results. This is shown in Fig. 4, where the blunt-body problem is computed solving the full Navier–Stokes equations, using the same upwind method (FDSPAN) as in the previous examples. In this case, the grid is composed of 40 cells in the radial direction and is clustered close to the cylinder wall, but the cells' aspect ratio in the bow shock region has been maintained equal to that of the inviscid computation. From these results, it is evident that one cannot rely on the natural viscosity to damp the numerical instability, because even for unpractically low Reynolds numbers, the solution is still affected by the carbuncle.

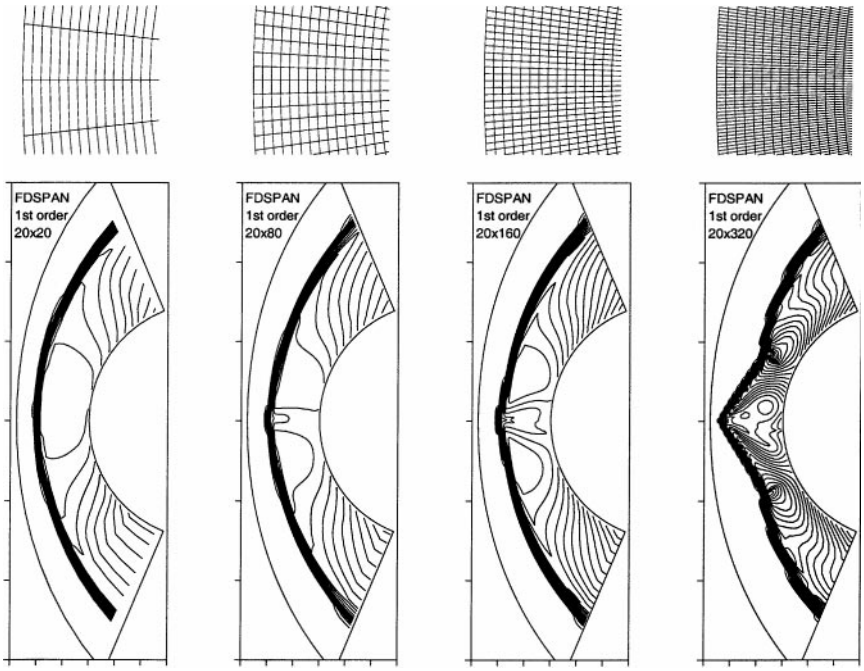

FIG. 2. Supersonic inviscid flow around a blunt body at $M_\infty = 20$ (density contours). Effect of the tangential refinement. An enlarged view of the grid in the region where the carbuncle occurs is shown above each result.

From these facts, which can easily be reproduced in simple numerical experiments, we have drawn some conclusions:

1. The instability is generated by solving the RP on those interfaces that are oriented with the unit vector parallel to the normal shock (those whose dimension is indicated as $\Delta\xi$ in Fig. 5); if the grid element is highly elongated in this direction, tangential to the shock, as

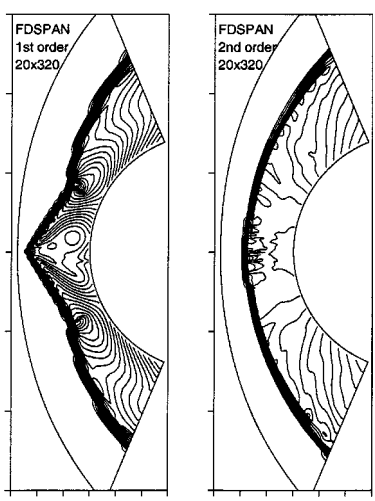

FIG. 3. Carbuncle in the supersonic inviscid flow around a blunt body at $M_\infty = 20$ (density contours). First-order (left) and second-order (right) results.

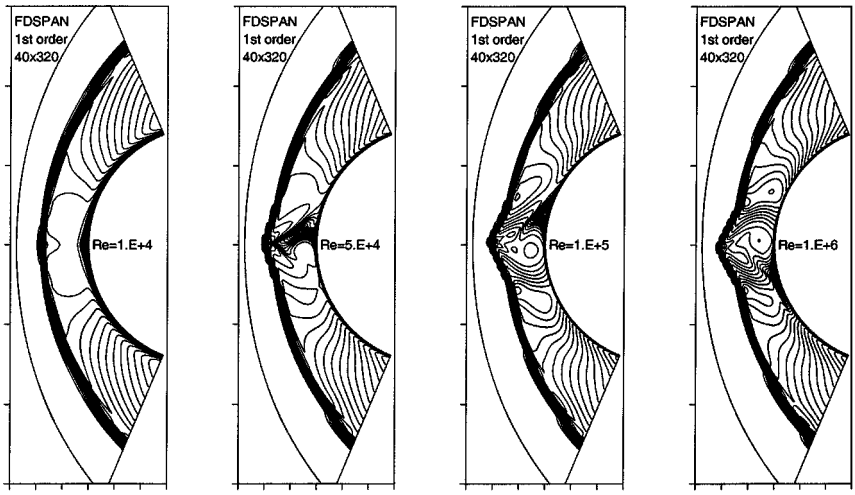

FIG. 4. Supersonic viscous flow around a blunt body at $M_\infty = 20$ (density contours). From left to right, the Reynolds number is equal to 10^4, $5 \cdot 10^4$, 10^5, and 10^6.

in case a of Fig. 5, the time step that will be used to integrate the conservation equations for that cell will be the one dictated by the Courant–Friedrichs–Lewy (CFL) condition related to the other surface, the one whose dimension is indicated as $\Delta\eta$. Therefore, the RP across the interfaces $\Delta\xi$ will be solved using a time step that is smaller than the one which should be necessary for them alone. In this way, some additional numerical diffusion is introduced into the fluxes across those surfaces and this explains why the carbuncle is less intense with this kind of grid aspect ratio. Conversely, if the situation is as depicted in case b of Fig. 5, the time step that will be used will be the one which is related directly to the interface with dimension $\Delta\xi$, so that no additional artificial diffusion will be introduced.

2. The carbuncle phenomenon is connected to those solutions of the RP that explicitly take into account the contact surface; this fact is usually shown by its occurrence in FDS approaches; the explicit treatment of the contact surface seems to be the essential point of the problem.

3. It is convenient to focus attention on the algorithms based on the first-order integration scheme [17]; in this case, the initial discontinuity of the RP shows its largest amplitude and the relevance of the upwind method to the carbuncle occurrence becomes more important, despite the higher numerical dissipation related to the first-order scheme.

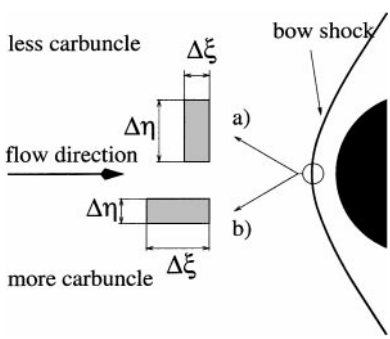

FIG. 5. Aspect ratio of the cells and carbuncle occurrence.

On the basis of these conclusions, it would seem convenient to start with an examination of the features and characteristics of upwind methods.

3. UPWIND METHODS

Upwind methods present the appealing feature of introducing the elements of the wave propagation phenomenology in the integration of conservation laws (CL). In their construction, the partial differential form of the governing equations (PDE) plays a fundamental role in estimating the flux over the surface that bounds the control volume considered by the CL.

For the purpose of reviewing different upwind methods, we examine the 1D inviscid problem and define the flux $F_{N+1/2}$ at the interface that separates two neighboring cells, N and $N+1$. The flux $F_{N+1/2}$ is estimated by solving an RP, that is, the evolution in time of an initial flow discontinuity (constructed with the initial data at N and $N+1$), in terms of propagating waves.

We consider a first group of upwind methods, where the flux $F_{N+1/2}$ is evaluated throughout the full and correct interaction between the initial data at the cells N and $N+1$. The RP is solved according to the three-wave model described by the PDE (evolution of smooth waves) and by the CL (jump conditions for propagating discontinuities). The initial data at N and $N+1$ contribute together to the development of two *acoustic* genuinely nonlinear waves (or shocks), related to the characteristic families $\lambda_{1,3} = u \mp a$, and of the *contact surface* linearly degenerated wave, associated to the characteristic $\lambda_2 = u$. This procedure, the *Riemann approach* as defined in [6], can be considered the direct heir of the work of Godunov [5] and represents the basic feature of the FDS methods. It is worthwhile to point out that the explicit treatment of the contact surface is the keynote of FDS methods.

The solution of the RP can be carried out exactly, through iterations based on the method of characteristics (MOC), matched to the proper jump conditions in the presence of discontinuities. However, to save computing time, approximate solvers of the RP have been proposed. Among these, mention should be made of the one suggested in [19] (FDSROE), an exact solver of a linearized definition of the RP, the one suggested in [15], which is an approximate solution of the actual RP, and the mirror image of the latter proposed in [16](FDSPAN).

In a second group of upwind methods, the flux $F_{N+1/2}$ is evaluated by adding the individual contributions of the cells N and $N+1$, where each contribution is estimated locally, in N or $N+1$, without the establishment of any mutual interaction between the two neighboring cells. These are the *flux-vector splitting* (FVS) methods, inspired by the *Boltzmann approach*, as suggested in [6]. The contact surface, which in some flow configurations may represent a strong discontinuity, is not treated explicitly and its content can be spread over two waves traveling in opposite directions. This leads to incorrect diffusion of the contact surface and the algorithm results tend to be highly dissipative in strongly rotational flows. Among the FVS methods, mention can be made of the original one proposed in [21] (FVSSW) and the subsequent one suggested in [24] (FVSVL).

The splitting method proposed in [3, 6] and known in the literature as HLL, or HLLE, is conceived as an FDS approach, but the contact surface is definitely ignored, as only the *acoustic* waves are taken into consideration. As a result, only a weak interaction between the cells N and $N+1$ exists in the determination of $F_{N+1/2}$ and the algorithm introduces a strong dissipation related to the intermediate wave.

In recent years, the *advection upstream splitting method* (AUSM) has been proposed. Here, the flux $F_{N+1/2}$ is considered as being composed of a "convective" part and a "pressure" part. The first is evaluated on the basis of a strong interaction between the N and $N+1$ cells, whereas, for the second, no interaction occurs. There are different versions of the AUSM method: one is based on a velocity splitting (AUSM-VEL) [11], a second one refers to a Mach number splitting (AUSM-M) [12], and a third one has been proposed more recently (AUSM+) [13].

With the exception of FDS methods, which explicitly account for the contact surface, none of the others reproduces a full and correct interaction between the initial data at N and $N+1$. Many suggestions can therefore be found in the literature, for methods that present these deficiencies, to restore the missing contact surface and thus the full interaction to estimate $F_{N+1/2}$. In the *hybrid upwind scheme* (HUS) [2], an FVS method is upgraded to the FDS level, by introducing the explicit treatment of the second wave; for our present analysis, we have reconstructed an HUS method by implementing elements from FDSPAN in FVSVL. The HLL method has also been modified to recover the missing contact surface, as indicated in [4] (HLLEM) or in [22] (HLLC). A restoration of the contact surface has also been worked out for the AUSM family (AUSMV and AUSMD) [25, 26]. We hereafter refer to these methods (HUS, HLLEM, HLLC, AUSMV, and AUSMD) as "mimes" of the FDS.

In the present paper, we report the results of numerical experiments obtained with FDSROE and FDSPAN for flux-difference splitting, with FVSSW and FVSVL for flux-vector splitting, with HLL (or HLLE), and with AUSM-VEL, AUSM-M, and AUSM+ for advection upstream splitting; as far as FDS mimes are concerned, we consider a HUS version (FDSPAN coupled to FVSVL), HLLC (where the wave velocities are determined from FDSPAN), and finally AUSMV and AUSMD.

4. TWO SIGNIFICANT EXAMPLES

In this section, we will show the results of numerical experiments carried out using different upwind methods on two significant examples.

The first example refers to the inviscid supersonic flow ($M_\infty = 20$) around a circular cylinder. The grid is shown in Fig. 6a and is composed of 20 radials and 320 tangential intervals; one should note that only one out of five grid lines is drawn in the picture. The mesh is very elongated in the radial direction to emphasize the effects of the carbuncle. As far as the boundary conditions are concerned, uniform upstream values are imposed on the outer radial boundary, impermeability is prescribed at the wall, and flow properties are extrapolated at the boundaries where the outflowing gas is supersonic. All the computations have been carried out with the plain first-order scheme and the same numerical treatment at the wall.

The results are reported in Fig. 6, in terms of density contour lines. We can observe that FDS methods (FDSROE in Fig. 6b and FDSPAN in Fig. 6c) exhibit a well-pronounced carbuncle, which also appears in the FDS mimes. The instability in HLLC in Fig. 6e is as intense as in FDS; AUSMD, in Fig. 6g, also shows a remarkable carbuncle. Somewhat better—although still unacceptable—results are obtained with HUS (Fig. 6d) and AUSMV (Fig. 6f). In contrast, FVS methods exhibit the complete absence of the instability (FVSVL in Fig. 6h); even the HLL splitting method is totally carbuncle-free, as is shown in Fig. 6i.

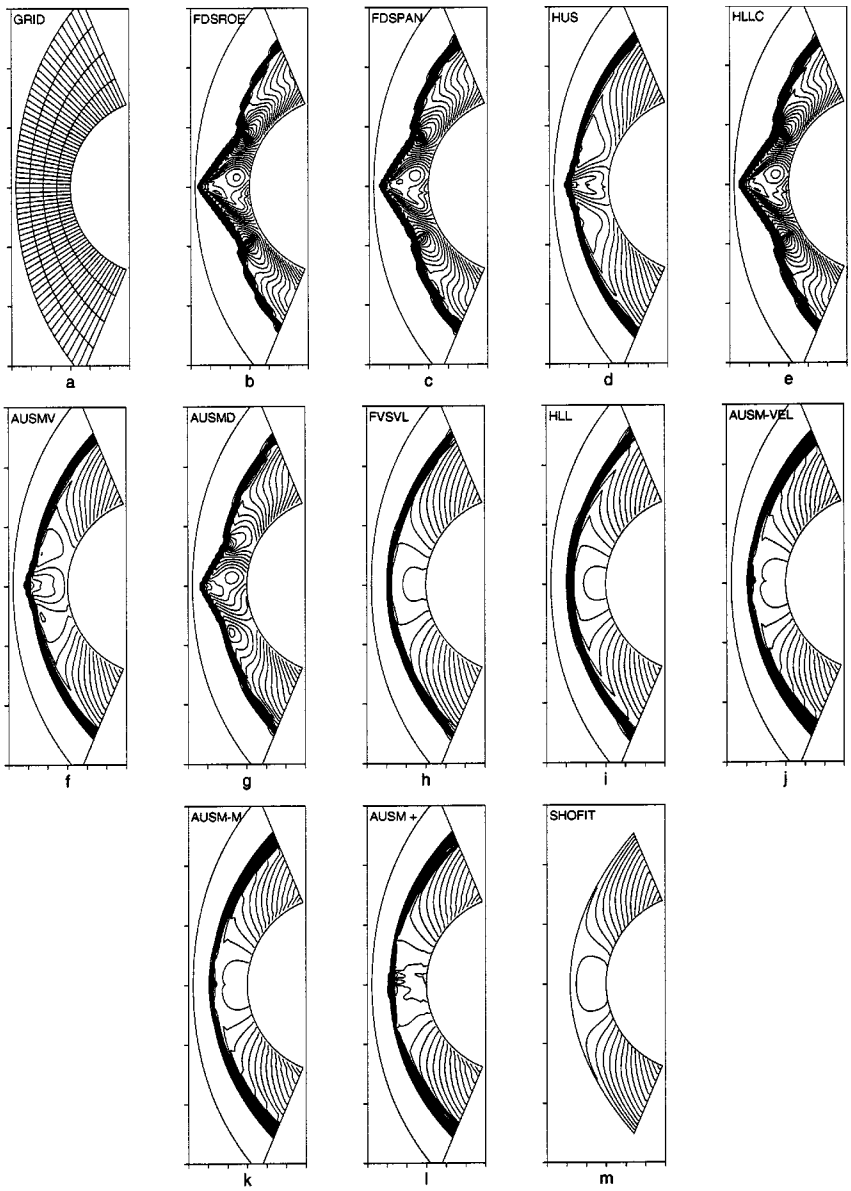

FIG. 6. Supersonic inviscid flow around a blunt body at $M_\infty = 20$ (density contours).

Moderate, but nevertheless disturbing, anomalies are presented by the remaining AUSM methods (AUSM-VEL in Fig. 6j, AUSM-M in Fig. 6k, and AUSM+ in Fig. 6l). One should note that density contour lines appear to be more sensitive in showing anomalies, whereas those related to the Mach number tend to attenuate the irregularity. Finally, the *shock-fitting technique* (SHOFIT), in the unusual matching with an FDS method (here FDSPAN), presents perfect results, as shown in Fig. 6m; as previously mentioned, this happens because the explicit treatment of the bow shock does not require any shock-capturing region.

From the results reported in Fig. 6, we can conclude that those methods that explicitly deal with the contact surface, by introducing a significant interaction between the initial data at N and $N + 1$, display clear evidence of the carbuncle phenomenon; in contrast,

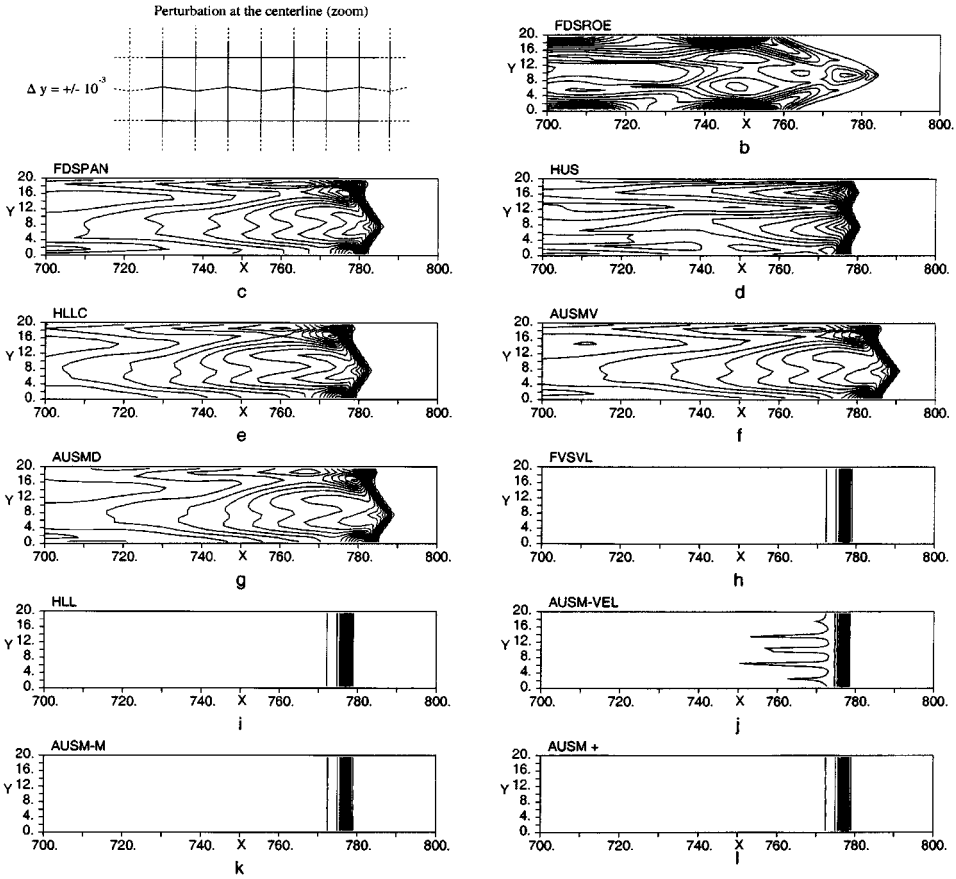

FIG. 7. Moving shock at $M_\infty = 6$ (density contours).

when such an interaction is barely taken into account, or even totally ignored, no carbuncle instability occurs. The AUSM versions present some intermediate behavior.

A second significant example is now considered [17]. A shock propagates down a straight duct, at the speed of $M_{\text{sh}} = 6.0$. The flow is inviscid. The grid has 800 cells along the duct and 20 in the transverse direction. Each cell is a square with unit side, except those on the centerline, which are distorted, as shown in Fig. 7a. The distortion, in fact, looks much more amplified there, since the one actually imposed presents a perturbation in the vertical side of $\Delta y = \pm 10^{-3}$, which would be undetectable at the correct scale. The example proposed in [17] would suggest a much smaller perturbation ($\Delta y = \pm 10^{-6}$), but a larger value has here been assumed to give more emphasis to the problem. Boundary conditions are prescribed as follows. The propagating shock is strong enough for the flow entering the duct at the inlet boundary to be supersonic: then, all the flow properties are prescribed here. In the attempt to simulate an infinitely long duct, nonreflecting simple wave boundary conditions are imposed at the outlet. The upper and lower boundaries are considered as solid walls except for the case taken into account at the end of Section 5, where periodicity conditions are imposed.

The shock begins its propagation from the left side of the duct, moving rightward with a perfectly plane shape. Some disturbances are induced on the centerline and, depending

on the method used, they can grow and deteriorate, or just remain confined. The numerical results are reported as density contour lines in Fig. 7 and show the shock in the right portion of the duct, and more specifically in the last 100 cells. We can observe the same kind of results that have already been seen in the blunt-body example. The FDS methods and their mimes show terrible shapes for the shock, once more justifying the carbuncle denomination. (Figs. 7b–g). The methods related to FVS and the HLL splittings do not present any deterioration (Figs. 7h, i). The AUSM methods also show slight instabilities here; the latter can be seen only for AUSM-VEL (Fig. 7j), but not for AUSM-M (Fig. 7k) or AUSM+ (Fig. 7l), but also become clearly visible in these cases, if the grid perturbation is raised to higher levels.

The results obtained in this second example are in agreement with those reported for the first one and confirm the previous conclusions on the performances to be expected from the different upwind methods.

5. ANALYSES OF THE LINEARIZED ALGORITHMS

We consider, in a 2D domain (x, y), two squared cells with unit side (N, M) and $(N, M+1)$, whose centers are located respectively at $x_{(N,M)}, y_{(N,M)}$ and at $x_{(N,M+1)} = x_{(N,M)}$, $y_{(N,M+1)} = y_{(N,M)} + 1$, and a gas flowing with the velocity $\mathbf{q} = u \cdot \mathbf{i} + v \cdot \mathbf{j}$. Uniform conditions are assumed, with normalized values $\rho_0 = 1$, $u_0 \neq 0$, $v_0 = 0$, and $p_0 = 1$. Density, shear velocity, and pressure perturbations $(\hat{\rho}, \hat{u}, \hat{p})$ are then prescribed and the flow properties $\rho = 1 \pm \hat{\rho}$, $u = u_0 \pm \hat{u}$, $v = 0$, and $p = 1 \pm \hat{p}$ are defined, with the sign $+$ or $-$ used respectively in the cell (N, M) or $(N, M+1)$ (Fig. 8). By considering the linearized form of the algorithm for the different methods, we evaluate the flux $\mathbf{G} = (\rho v, \rho uv, p + \rho v^2, v \cdot (p + e))^T$ at the interface $(N, M + 1/2)$. One should note that, in this problem, v is the velocity component normal to the interface, while u is acting as the tangential, or shear, velocity. The results of this analysis are reported in Table I. Appendix A shows how they can be obtained for some of the methods considered.

The first line refers to the method of characteristics (MOC) and represents the "physically" correct reference solution (in the sense of full consistency with the Euler governing

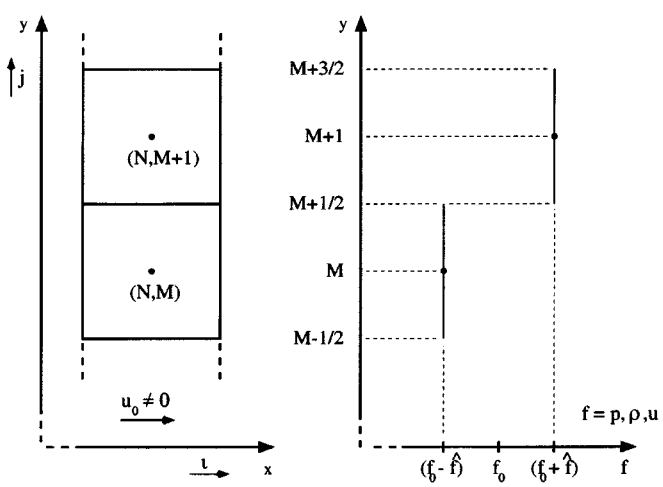

FIG. 8. Analysis of the linearized algorithms: the 2D domain.

TABLE I
RP Solution with Different Upwind Methods

	$(G_1)_{M+1/2}$	$(G_2)_{M+1/2}$	$(G_3)_{M+1/2}$	$(G_4)_{M+1/2}$
MOC, FDSROE, FDSPAN, HLLC	$\left(+\frac{1}{\sqrt{\gamma}}\right)\hat{p}$	$\left(+\frac{u_0}{\sqrt{\gamma}}\right)\hat{p}$	1	$\left(+\frac{\sqrt{\gamma}}{\gamma-1}+\frac{{u_0}^2}{2\sqrt{\gamma}}\right)\hat{p}$
FVSSW	$\left(+\frac{1}{2\sqrt{\gamma}}\right)(\hat{\rho}+\hat{p})$	$\left(+\frac{u_0}{2\sqrt{\gamma}}\right)\left(\hat{\rho}+2\frac{\hat{u}}{u_0}+\hat{p}\right)$	1	$\left(+\frac{\sqrt{\gamma}}{2(\gamma-1)}\right)(-\hat{\rho}+3\hat{p})+\left(+\frac{{u_0}^2}{4\sqrt{\gamma}}\right)\left(\hat{\rho}+4\frac{\hat{u}}{u_0}+\hat{p}\right)$
FVSVL	$\left(+\frac{\sqrt{\gamma}}{4}\right)(\hat{\rho}+\hat{p})$	$\left(+\frac{u_0\sqrt{\gamma}}{4}\right)\left(\hat{\rho}+2\frac{\hat{u}}{u_0}+\hat{p}\right)$	1	$\left(+\frac{\sqrt{\gamma}\gamma}{2(\gamma^2-1)}\right)(-\hat{\rho}+3\hat{p})+\left(+\frac{{u_0}^2\sqrt{\gamma}}{8}\right)\left(\hat{\rho}+4\frac{\hat{u}}{u_0}+\hat{p}\right)$
HUS	$\left(+\frac{(\gamma+1)}{4\sqrt{\gamma}}\right)\hat{p}$	$\left(+\frac{\gamma+1}{4}\frac{u_0}{\sqrt{\gamma}}\right)\hat{p}$	1	$\left(+\frac{\sqrt{\gamma}}{2}\frac{(3\gamma-1)}{(\gamma^2-1)}+\frac{{u_0}^2}{8}\frac{(\gamma+1)}{\sqrt{\gamma}}\right)\hat{p}$
HLL	$(+\sqrt{\gamma})\hat{\rho}$	$(+u_0\sqrt{\gamma})\left(\hat{\rho}+\frac{\hat{u}}{u_0}\right)$	1	$\left(+\frac{{u_0}^2\sqrt{\gamma}}{2}\right)\hat{\rho}-(-{u_0}^2\sqrt{\gamma})\frac{\hat{u}}{u_0}+\left(\frac{\sqrt{\gamma}}{\gamma-1}\right)\hat{p}$
AUSM-VEL	$\left(+\frac{\sqrt{\gamma}}{4}\right)(-\hat{\rho}+\hat{p})$	$\left(+\frac{u_0\sqrt{\gamma}}{4}\right)(-\hat{\rho}+\hat{p})$	1	$\left(+\frac{\sqrt{\gamma}\gamma}{4(\gamma-1)}+\frac{{u_0}^2\sqrt{\gamma}}{8}\right)(-\hat{\rho}+\hat{p})$
AUSM-M, AUSM+	0	0	1	0
AUSMD, AUSMV	$\left(+\frac{\sqrt{\gamma}}{2}\right)\hat{p}$	$\left(+\frac{u_0\sqrt{\gamma}}{2}\right)\hat{p}$	1	$\left(+\frac{\sqrt{\gamma}\gamma}{2(\gamma-1)}+\frac{{u_0}^2\sqrt{\gamma}}{4}\right)\hat{p}$

equations). Clearly, FDS methods give the same result as the MOC (FDSROE and FDSPAN solvers coincide in this small-perturbation analysis). Only the pressure perturbation ($\hat{p} \neq 0$) affects the flux; density and shear velocity perturbations ($\hat{\rho} \neq 0$ and $\hat{u} \neq 0$) have no effect on the flux, just as physically required by the Eulerian model. FDS mimes (HLLC, HUS, AUSMD, and AUSMV in Table I) behave in the same or in a similar way.

Conversely, we can observe that, in FVS methods, the predicted flux is sensitive not only to the pressure perturbation but also to density and shear velocity perturbations. The two methods, FVSSW and FVSVL, present a similar sensitivity to $\hat{\rho}$, $\hat{u}$, and $\hat{p}$ and both give nonphysical results.

Even the HLL method presents a behavior that is not consistent with the solution of the Euler equations, as the flux is influenced by density and shear velocity perturbations.

Finally, AUSM methods exhibit particular behavior. In the AUSM-VEL version (in this analysis the split of the velocity is on the v component), the flux $\mathbf{G}$ at the interface $(N, M+1/2)$ reacts to $\hat{p}$ (with only a slight variation of the coefficient compared to the MOC); it does not respond to the shear velocity perturbation $\hat{u}$ (as in the MOC) but is sensitive to $\hat{\rho}$ with the sign of some coefficients opposite to the one that appears in FVS and HLL. This last point may anticipate a somewhat antidissipative behavior of this method. The AUSM-M and AUSM+ versions show a very unusual reaction; they do not respond to any perturbation (pressure, density, or shear velocity). Although this is correct for density and shear velocity,

it is clearly incorrect for pressure, where we should expect a physical influence on the flux due to the propagation of waves.

One should note that the results reported in Table I are fully consistent with the predictions seen in Fig. 6 and Fig. 7, in the sense that those methods that do behave correctly according to the analysis of Table I are strongly affected by numerical instabilities, whereas those that are highly (and incorrectly) dissipative, as far as density and shear velocity perturbations are concerned, appear as carbuncle-free.

The results of the analysis shown in Table I can be used to develop a further study, defined in [17] as the odd–even decoupling problem. We consider the previously seen uniform flow ($\rho_0 = 1, u_0 \neq 0, v_0 = 0, p_0 = 1$) over the rectangular domain (x, y), described by squared cells of unit side. We introduce initial perturbations $\hat{\rho}^\circ$, $\hat{u}^\circ$, $\hat{p}^\circ$ (the apex is the time step counter) in an odd–even fashion along the coordinate y, so that the flow is described by $\rho^\circ = 1 \pm \hat{\rho}^\circ, u^\circ = u_0 \pm \hat{u}^\circ, v^\circ = 0, p^\circ = 1 \pm \hat{p}^\circ$, where the $+$ sign refers to the cell (N, M) and the $-$ sign to the neighboring cells $(N, M-1)$ and $(N, M+1)$. Periodic boundary conditions are prescribed in the y direction; moreover, the flow is assumed to be uniform along x, so that the problem is reduced to one dimension. The results of Table I are then used to perform the integration of the conservation laws, using the plain first-order scheme. This kind of analysis is developed in [17] for density and pressure perturbations ($\hat{\rho}^\circ \neq 0$ and $\hat{p}^\circ \neq 0$), with reference to the FDSROE and HLL methods. We also introduce the shear velocity perturbation ($\hat{u}^\circ \neq 0$) and extend the analysis to all the previously mentioned methods. Starting from the above set of initial perturbations $\hat{\rho}^\circ$, $\hat{u}^\circ$, $\hat{p}^\circ$ ($\hat{v}^\circ = 0$), we describe the integration process by the recursive formulas that are reported in Table II. Appendix B shows how these formulas are obtained from Table I for some of the methods considered. Perturbations at step $K+1$ ($\hat{\rho}^{K+1}$, $\hat{u}^{K+1}$, $\hat{p}^{K+1}$) are evaluated on the basis of the data of the previous step K ($\hat{\rho}^K$, $\hat{u}^K$, $\hat{p}^K$). Since we have assumed the initial perturbation of the velocity component along y to be null ($\hat{v}^\circ = 0$), $\hat{v}^{K+1} = \hat{v}^K = \hat{v}^\circ = 0$ results in all the methods. Therefore, there are no recursive formulas for $\hat{v}^K$ in Table II. The time step of the integration (Δt) appears in the Courant number $\nu = \sqrt{\gamma}\frac{Dt}{Dy}$, where γ is the ratio of the specific heats and is equal to 1.4 for air.

The MOC (used in the original Godunov suggestion), FDSROE, FDSPAN, and HLLC methods, since they all present the same response to perturbations in Table I, naturally give the same result in Table II. It is important to notice that, if the initial pressure is uniform ($\hat{p}^\circ = 0$), but the density and shear velocity perturbations are not zero ($\hat{\rho}^\circ \neq 0$, $\hat{u}^\circ \neq 0$), the initially perturbed configuration is preserved (Fig. 9), as should be physically expected in the framework of the Euler equations. Only the pressure perturbation ($\hat{p}^\circ \neq 0$) induces flow variations through acoustic waves that travel up and down along y. In Fig. 10, this pressure perturbation is flattened because the Courant number used is lower than 1.0 ($\nu = 0.2$). In the case of $\hat{\rho}^\circ = 0$, the density is isoentropically perturbed until, as $K \to \infty$, $\hat{\rho}^\infty = -\hat{p}^\circ/\gamma$ (Fig. 10). In all the cases, the initial shear velocity perturbation $\hat{u}^\circ$ remains unaltered: $\hat{u}^\infty = \hat{u}^K = \hat{u}^\circ$. The HUS, AUSMV, and AUSMD methods provide evolutions of the perturbations that are very similar to FDS methods, as the recursive formulas have the same structure, with only slightly different coefficients.

The FVS methods (FVSSW and FVSVL are almost identical) damp any perturbation. The shear velocity perturbation ($\hat{u}$) decays independently from the others: $\hat{u}^\infty = 0$. However, pressure and density perturbations interact with each other (Figs. 11 and 12): an initial density perturbation ($\hat{\rho}^\circ \neq 0$) can also induce a temporary pressure perturbation ($\hat{p}^K \neq 0$), even for an initially uniform pressure ($\hat{p}^\circ = 0$). The final configuration, reached as $K \to \infty$,

TABLE II
Integration with the Linearized Form of the Different Methods

MOC,	$\hat{\rho}^{K+1} =$	$\hat{\rho}^K$		$+$		$\left(-\frac{2\nu}{\gamma}\right)\hat{p}^K$
FDSROE,	$\hat{u}^{K+1} =$		$\hat{u}^K$			
FDSPAN,	$\hat{p}^{K+1} =$					$(1-2\nu)\hat{p}^K$
HLLC						
FVSSW	$\hat{\rho}^{K+1} =$	$\left(1-\frac{\nu}{\gamma}\right)\hat{\rho}^K$		$+$		$\left(-\frac{\nu}{\gamma}\right)\hat{p}^K$
	$\hat{u}^{K+1} =$		$\left(1-\frac{2\nu}{\gamma}\right)\hat{u}^K$			
	$\hat{p}^{K+1} =$	$(\nu)\hat{\rho}^K$				$(1-3\nu)\hat{p}^K$
FVSVL	$\hat{\rho}^{K+1} =$	$\left(1-\frac{\nu}{2}\right)\hat{\rho}^K$		$+$		$\left(-\frac{\nu}{2}\right)\hat{p}^K$
	$\hat{u}^{K+1} =$		$(1-2\nu)\hat{u}^K$			
	$\hat{p}^{K+1} =$	$\left(\nu\frac{\gamma}{\gamma+1}\right)\hat{\rho}^K$				$\left(1-3\nu\frac{\gamma}{\gamma+1}\right)\hat{p}^K$
HUS	$\hat{\rho}^{K+1} =$	$\hat{\rho}^K$		$+$		$\left(-\frac{\nu}{2}\frac{\gamma+1}{\gamma}\right)\hat{p}^K$
	$\hat{u}^{K+1} =$		$\hat{u}^K$			
	$\hat{p}^{K+1} =$					$\left(1-\nu\frac{3\gamma-1}{\gamma+1}\right)\hat{p}^K$
HLL	$\hat{\rho}^{K+1} =$	$(1-2\nu)\hat{\rho}^K$				
	$\hat{u}^{K+1} =$		$(1-2\nu)\hat{u}^K$			
	$\hat{p}^{K+1} =$					$(1-2\nu)\hat{p}^K$
AUSM-VEL	$\hat{\rho}^{K+1} =$	$\left(1+\frac{\nu}{2}\right)\hat{\rho}^K$		$+$		$\left(-\frac{\nu}{2}\right)\hat{p}^K$
	$\hat{u}^{K+1} =$		$\hat{u}^K$			
	$\hat{p}^{K+1} =$	$\left(\frac{\nu\gamma}{2}\right)\hat{\rho}^K$				$\left(1-\frac{\nu\gamma}{2}\right)\hat{p}^K$
AUSM-M,	$\hat{\rho}^{K+1} =$	$\hat{\rho}^K$				
AUSM+	$\hat{u}^{K+1} =$		$\hat{u}^K$			
	$\hat{p}^{K+1} =$					$\hat{p}^K$
AUSMD,	$\hat{\rho}^{K+1} =$	$\hat{\rho}^K$		$+$		$(-\nu)\hat{p}^K$
AUSMV	$\hat{u}^{K+1} =$		$\hat{u}^K$			
	$\hat{p}^{K+1} =$					$(1-\nu\gamma)\hat{p}^K$

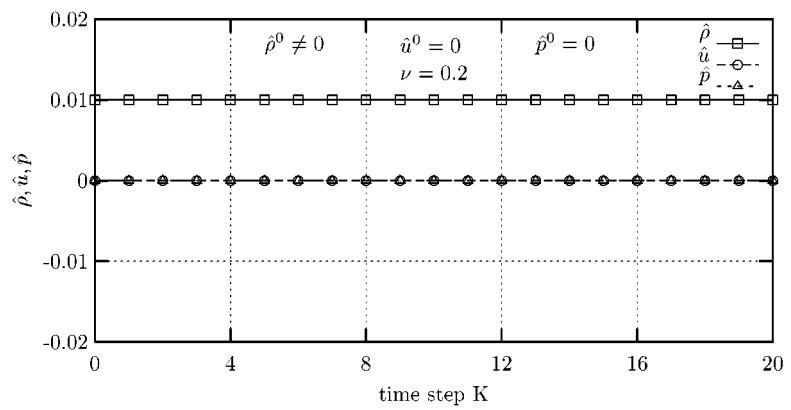

FIG. 9. Odd–even decoupling problem: MOC, FDSROE, FDSPAN, and HLLC reactions to a density perturbation.

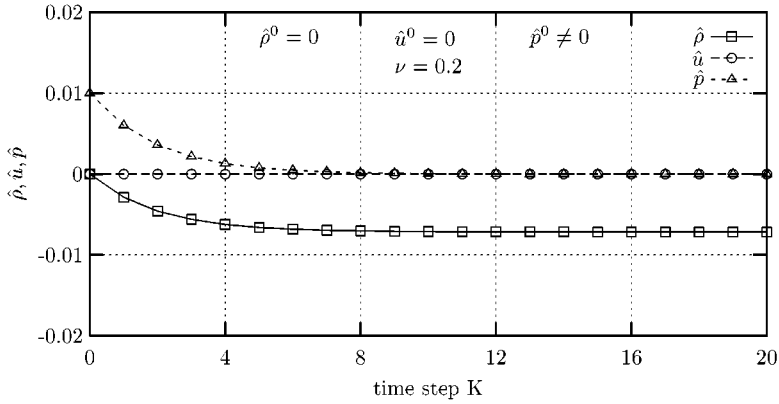

FIG. 10. Odd–even decoupling problem: MOC, FDSROE, FDSPAN, and HLLC reactions to a pressure perturbation.

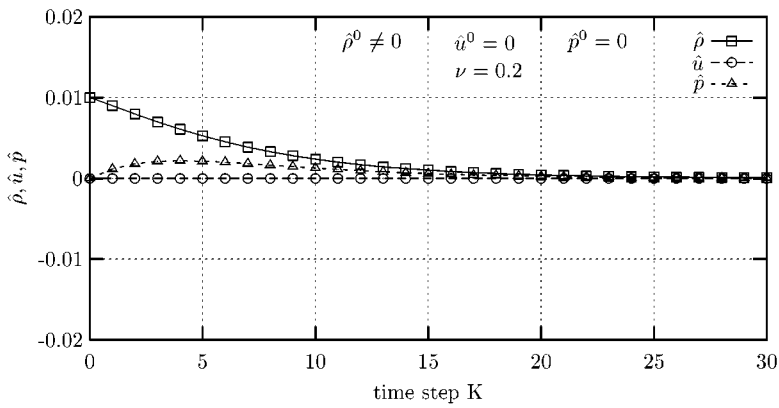

FIG. 11. Odd–even decoupling problem: FVSVL reaction to a density perturbation.

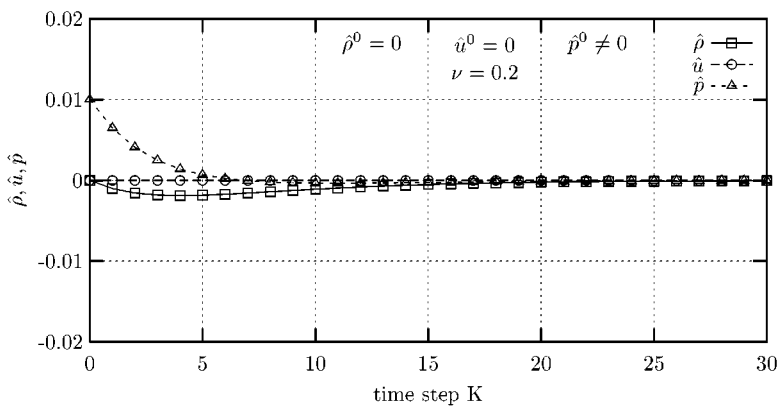

FIG. 12. Odd–even decoupling problem: FVSVL reaction to a pressure perturbation.

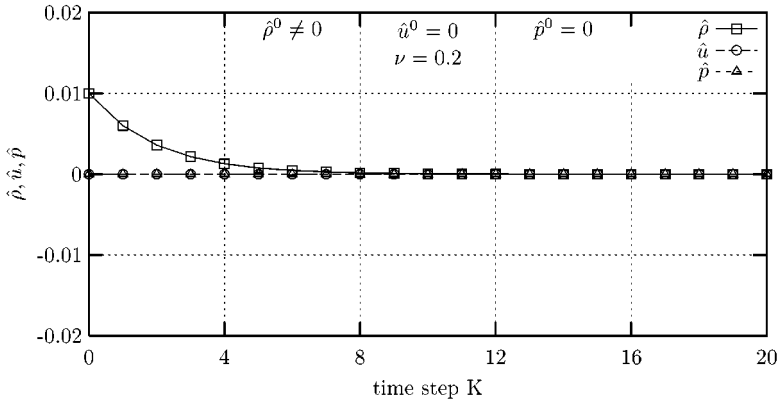

FIG. 13. Odd–even decoupling problem: HLL reaction to a density perturbation.

is always uniform: $\hat{\rho}^\infty = \hat{p}^\infty = 0$ (Fig. 12). This picture is not consistent with the governing equations, as is clearly shown in practical computations of highly rotational flows, where a fictitious dissipation is introduced by these methods.

In the HLL method, each perturbation is damped, but independently from the others; also, the behavior is incorrect (Figs. 13 and 14).

The various versions of the AUSM method present different evolutions of the perturbations. In all the versions (AUSM-VEL, AUSM-M, and AUSM+), the shear velocity perturbation remains unaltered, without any coupling to other perturbations ($\hat{u}^\infty = \hat{u}^K = \hat{u}^\circ$). The picture becomes different for pressure and density evolutions. In AUSM-VEL, the sign of the coefficients in the recursive formulas generates a curious situation when relating pressure and density. If we assume, for instance, an initially uniform pressure distribution ($\hat{p}^\circ = 0$) and a nonzero density perturbation ($\hat{\rho}^\circ \neq 0$), instead of preserving this condition, the algorithm generates a transient, where not only does the density evolve, but a pressure perturbation is also generated. Asymptotically, the transient moves toward a steady configuration for the perturbations, and it can be recognized that, as $K \to \infty$, one obtains $\hat{\rho}^\infty = \hat{p}^\infty = \frac{\gamma}{\gamma-1}\hat{\rho}^\circ$. The density perturbation is amplified by a factor of 3.5 (for $\gamma = 1.4$) and an equal pressure perturbation is generated (Fig. 15). A similar result is also obtained

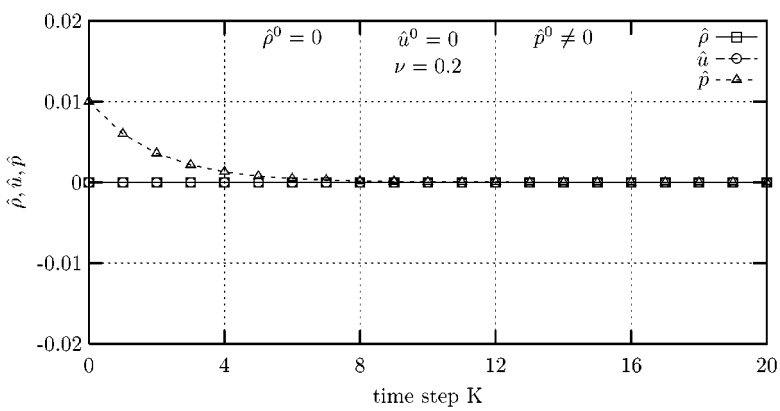

FIG. 14. Odd–even decoupling problem: HLL reaction to a pressure perturbation.

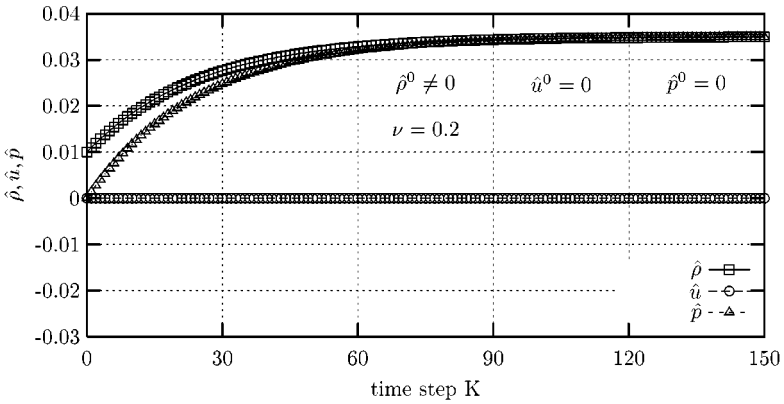

FIG. 15. Odd–even decoupling problem: AUSM-VEL reaction to a density perturbation.

for an initially perturbed pressure ($\hat{p}^\circ \neq 0$) and uniform density ($\hat{\rho}^\circ = 0$). In this case, both pressure and density perturbations increase to $\hat{\rho}^\infty = \hat{p}^\infty = \hat{p}^\circ/(1-\gamma)$ (Fig. 16). This kind of result could already have been anticipated in the analysis summarized in Table I. The behavior of AUSM-M and AUSM+ methods can be easily estimated in advance from Table I; no reaction of the flux was predicted there and, therefore, all the perturbations in Table II remain unaffected, without any mutual interaction (Figs. 17 and 18).

These results obtained for the AUSM versions are confirmed by practical numerical experiments, where pressure oscillations are observed inside boundary-layer flows with severe transverse density gradients (see, for instance, [9, 18, 23]). We have also experimented with such behavior in our own numerical tests.

The recursive formulas of Table II can provide some insight into the generation and development of carbuncle instabilities. In [17] we read that, for FDS methods, "if the pressure field is continuously perturbed in a systematic manner, no matter how small the pressure perturbations, $\hat{\rho}$ will grow without bound, albeit slowly." In the first previously seen example, the blunt-body flow (Fig. 6), the round-off error encountered in evaluating the flow in the uniform region ahead of the bow shock systematically generates pressure perturbations which are greatly amplified throughout the numerical transition of the captured shock. In

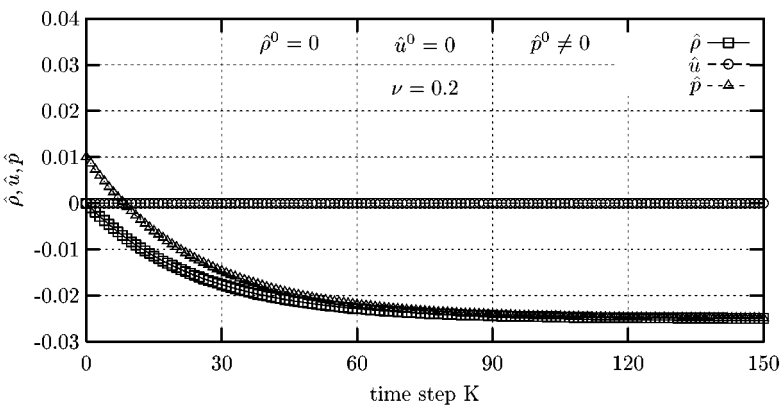

FIG. 16. Odd–even decoupling problem: AUSM-VEL reaction to a pressure perturbation.

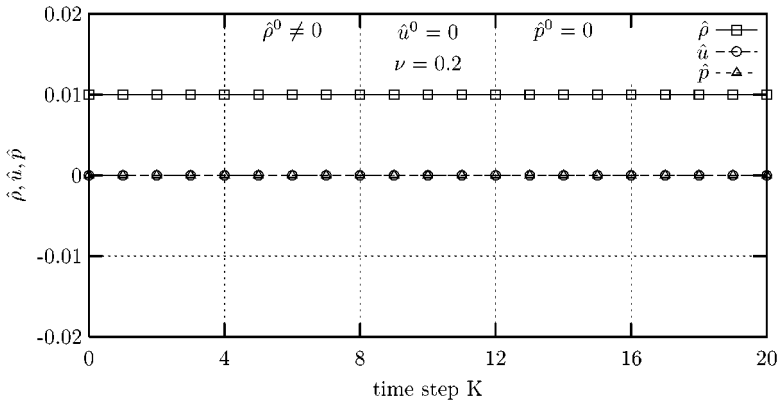

FIG. 17. Odd–even decoupling problem: AUSM-M and AUSM+ reactions to a density perturbation.

the second example of the shock propagating along the channel, the grid distortion at the centerline generates amplified pressure perturbations inside the numerically captured shock. The recursive formulas show that, for FDS and mime methods, the systematically generated pressure perturbations tend to be damped, but this process generates density perturbations, which are preserved and systematically grow. In contrast, with FVS methods, both the pressure and density perturbations are damped, as well as in the HLL method.

In synthesis, according to our analysis and with reference to the carbuncle problem, it would be possible to categorize FDS methods into the following four types.

a. Strong carbuncle prone schemes. These are schemes where pressure perturbations damp out but meanwhile create density perturbations that remain constant (MOC, FDSROE, FDSPAN, HLLC, HUS, AUSMD, and AUSMV).

b. Light carbuncle prone schemes. In these schemes pressure perturbations remain constant and do not interact with density perturbations, which also remain constant (AUSM-M and AUSM+).

c. Carbuncle-free schemes. In these schemes density perturbations damp out, with or without mutual interacion with pressure perturbations (FVSSW, FVSVL, and HLL).

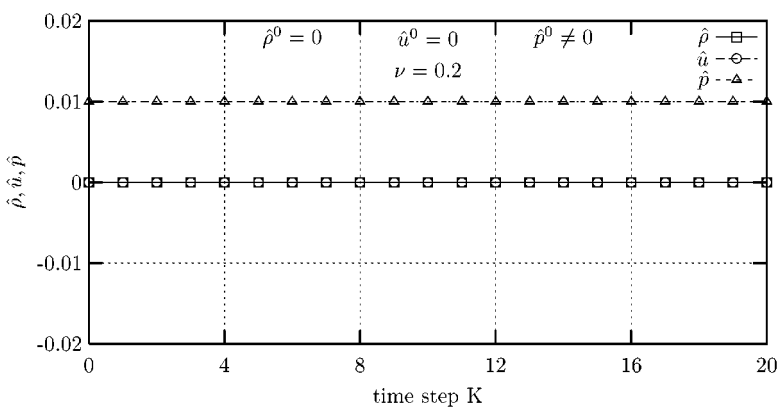

FIG. 18. Odd–even decoupling problem: AUSM-M and AUSM+ reactions to a pressure perturbation.

d. The AUSM-VEL scheme. This is the only scheme where both pressure and density perturbations induce a disturbance, which increases to a finite level, in the other variable; this mechanism produces the carbuncle, but the coupling between the two variables is such that the magnitude of the phenomenon is much less intense than for schemes belonging to category a.

We would like to point out that the previously described analyses require the linearization of the algorithm about $v_0 = \hat{v}^0 = 0$: this is a rather significant situation in the context of the carbuncle problem, since it reproduces the conditions where the carbuncle instability increases; therefore, the analyses are very relevant to the present study.

Moreover, the analyses can provide forewarnings on how a proposed algorithm is going to perform in practical computations with minimal efforts and without the need of carrying out full numerical experiments. For instance, it has been suggested in [14] that AUSMV and AUSMD be modified by defining a certain function $f = 1/\rho$ instead of a previous definition $f = p/\rho$ (see Eq. 32 in [25]). By adopting the previously presented analyses, it can be shown that with this modification AUSMV and AUSMD reduce to the behavior of AUSM-M or AUSM+. The two analyses can anticipate the numerical results shown in Fig. 2 of [14] and have been fully confirmed in our specific numerical experiments related to the examples of Figs. 6 and 7.

Our analyses can be generalized to the case with $v_0 \neq 0$, when the uniform flow runs diagonally on the (x, y) domain. This extension clarifies why the carbuncle occurs about normal shock waves and is only confined to the front region of the blunt-body flow in Fig. 6, without propagating above or below the symmetry line. The recursive formulas obtained for FDS methods, in cases when $v_0 \neq 0$ and the corresponding perturbation $\hat{v}^K \neq 0$ is introduced, are reported in Table III.

The presence of $v_0 \neq 0$ promotes the generation of a perturbation $\hat{v}^K$, even though $\hat{v}^\circ = 0$, for a prescribed perturbation $\hat{p}^\circ \neq 0$. However, the main effect of $v_0 \neq 0$ is the introduction of damping terms so that any kind of perturbation, initially prescribed or generated during a transient, disappears asymptotically in time (Figs. 19 and 20). The damping processes due to $v_0 \neq 0$ are purely dissipative and their magnitude increases with v_0; these facts contribute to confine the carbuncle instability in the neighborhood of the symmetry line of the blunt body.

The effects of $v_0 \neq 0$ are also quite evident in the second example, where a shock propagates along a channel: the dissipation introduced by a finite value of v_0 (a simulation of an oblique shock) tends to clean the distorted front of the shock and the irregularities of Fig. 7c (FDSPAN) are totally removed for $v_0 = 0.35$, as proved by our numerical experiments (Fig. 21). As anticipated in the previous section, periodicity conditions along the

TABLE III
Recursive Formulas with $v_0 \neq 0$ for FDS Methods

$\hat{\rho}^{K+1} =$	$\left(1 - 2\nu\frac{v_0}{\sqrt{\gamma}}\right)\hat{\rho}^K$	$+$	$\left(-2\nu\frac{v_0}{\sqrt{\gamma}}\right)\frac{\hat{v}^K}{\sqrt{\gamma}}$			$+$	$\left(2\frac{\nu}{\gamma}\left(\frac{v_0}{\sqrt{\gamma}} - 1\right)\right)\hat{p}^K$
$\hat{v}^{K+1} =$			$(1 - 2\nu)\hat{v}^K$			$+$	$\left(-2\frac{\nu}{\sqrt{\gamma}}\frac{v_0}{\sqrt{\gamma}}\right)\hat{p}^K$
$\hat{u}^{K+1} =$				$\left(1 - 2\nu\frac{v_0}{\sqrt{\gamma}}\right)\hat{u}^K$			
$\hat{p}^{K+1} =$			$\left(-2\nu\gamma\frac{v_0}{\sqrt{\gamma}}\right)\frac{\hat{v}^K}{\sqrt{\gamma}}$			$+$	$(1 - 2\nu)\hat{p}^K$

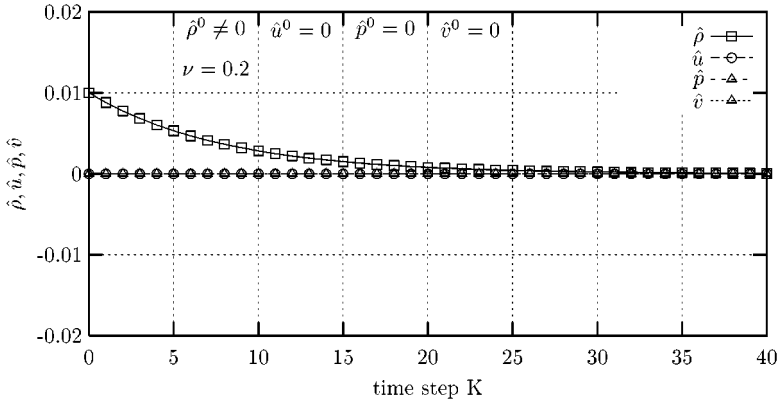

FIG. 19. Odd–even decoupling problem: FDS methods reaction to a density perturbation in the case of $v_0 \neq 0$ ($v_0 = 0.35$).

coordinate y are now imposed on the upper and lower boundaries of the duct. The dissipation introduced by $v_0 \neq 0$ is well known in the numerical prediction of the propagation of a contact surface in a 1D problem using FDS methods or mimes: if the flow is at rest, a contact surface retains its original sharpness, while in the presence of a propagation velocity, the original discontinuity is continuously smoothed.

6. CURES FOR THE CARBUNCLE

Highly rotational flows, which are typical of high-speed-regimes, are accurately predicted with upwind methods of the FDS family. Unfortunately, the deep sensitivity that these methods display when dealing with the contact surface represents a source of dangerous instabilities. Since the problem is not only of academic relevance but mainly of practical interest, suggestions have been proposed in the literature to overcome such a critical point, both to understand the nature of the deficiency and to recommend remedies. Curing methods

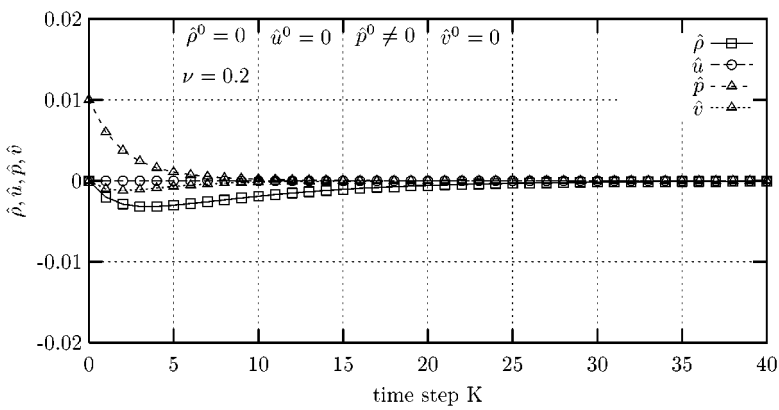

FIG. 20. Odd–even decoupling problem: FDS method reaction to a pressure perturbation in the case of $v_0 \neq 0$ ($v_0 = 0.35$).

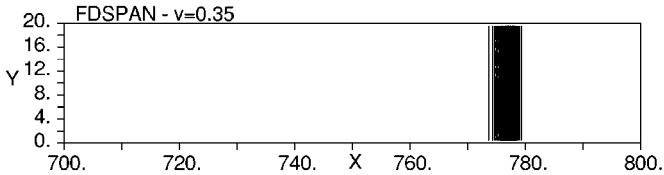

FIG. 21. Shock wave moving in a flow with a velocity component in the y direction (density contours).

proceed normally from three observations, as previously discussed. First, the carbuncle appears inside the zone of the numerical capture of a plane shock wave which is well aligned with a grid line. Second, the carbuncle originates when the flux across the interface normal to the shock itself is evaluated. Third, the source of the carbuncle has to be ascribed to FDS or "FDS mime" methods. By focusing attention on these facts, cures or remedies can be envisaged.

In [17] the following procedure is suggested. Each computational cell is inspected and the difference between the local pressure and its level in any of the surrounding cells is estimated. If such a difference overcomes a threshold value, the cell is flagged. In computing the flux on the interface between two flagged cells, the algorithm is switched from FDSROE, which is always used as the basic method, to HLL. The use of the latter method, which is a dissipative one, is confined to the restricted area where the shock is captured and will not generate spurious dissipations in strongly rotational flows. This cure is very efficient, as proved by the results reported in [17]; however, the empirical assumption of the threshold limit and the use of two totally different methods inside the code may not be so attractive.

A similar procedure is proposed in [25], but with some differences. Here, the detection of critical cells is carried out by looking at the sign of the speed of acoustic characteristics in any couple of adjacent cells. When a sonic transition through a compression is detected across a given interface, the algorithm is then switched from an FDS (or similar) method to a dissipative one, to compute the flux over the neighboring perpendicular interfaces. In [25], the basic method can be either AUSMDV (a blend of AUSMD and AUSMV) or FDSROE. The partner dissipative schemes used in the switching are respectively FVS (Hänel version [7]) and HLL. Even in this case, the cure is very efficient, as we have also experimented in our numerical exercises by matching the basic method FDSPAN and the dissipative FVSVL one. However, we have noted that the criterion used to detect the sonic line embedded in the captured shock, that is, the change in sign of characteristic speeds (Eq. 39 in [25]), is correct for shocks at rest, but it can fail for propagating shocks. However, it should be recalled that the detection of moving shocks, typically performed in shock-fitting techniques, has always been a critical point. Finally, as noticed for the previous cure [17], the introduction of a second method into the algorithm may be not attractive, especially in flows characterized by high-temperature effects.

The cure proposed in [20] offers interesting suggestions, because it does not require the introduction of an alternative dissipative scheme but retains the same basic method, in particular FDSROE, with some variable dissipation injected into the algorithm in connection to specific waves. The curing process is as follows. At any interface $(N, M + 1/2)$ that separates the cells (N, M) and $(N, M + 1)$, the maximum difference between the characteristic speeds computed in the cell centers is evaluated and its magnitude is introduced into that variation of the algorithm known as the *entropy fix* [8]. One should note that this operation is performed for all three waves and is not limited to the acoustic ones (as in [8]) for the specific

purpose of avoiding the formation of an expansion shock. This procedure already provides a reduction of the instability, but not enough, since it is not applied to the proper locations. It has therefore been suggested in [20] that the difference of the characteristic speeds be evaluated not only at the interface $(N, M+1/2)$ but also at the neighboring interfaces $(N-1/2, M)$ $(N+1/2, M)$, $(N-1/2, M+1)$, and $(N+1/2, M+1)$. The analysis is thus developed on a H-structure of interfaces about the central one $(N, M+1/2)$ and the parameter to be introduced into the *entropy fix* at the interface $(N, M+1/2)$ is assumed to be the maximum of the differences of the characteristic speeds across the five interfaces. The detection method devised to introduce numerical dissipation at the interface $(N, M+1/2)$ looks quite similar to the one reported in [25], but it does not require the identification of a sonic line and recognizes only sharp transitions of flow properties. Moreover, the detection does not introduce the abrupt switch to a partner dissipative algorithm but injects a variable level of dissipation into the basic algorithm that is related to the magnitude of the difference of the characteristic speeds. The results reported in [20] show that this cure is also very efficient. However, we should note that, in the case of a parallel streamlines flow with a severe transverse density gradient ($\rho_{N,M+1} \neq \rho_{N,M}$, as usually found in a high-speed flow boundary layer), the difference of the speed of sound across the interface $(N, M+1/2)$ parallel to the streamlines induces an incorrect dissipation at the interface.

A further interesting cure is proposed in [1]. Here, the basic algorithm is HLLEM, a version of HLL, which recovers the contact surface by introducing antidiffusive terms related to the second characteristic. The HLLEM method is obviously affected by the carbuncle phenomenon. The attractive feature of this cure is that only a local analysis is required and that there is no need to analyze the surrounding computational area, as in the previous prescriptions. Attention is focused on the intermediate state of the primitive variables when solving the RP, at a given interface, with the dissipative HLL scheme. If these values do not over- or undershoot the initial values of the RP, then, those obtained with HLLEM should not over- or undershoot either. If they do, the situation is considered potentially dangerous as far as the carbuncle phenomenon is concerned and the antidiffusive terms are limited to avoid any over- or undershooting. The resulting method, called HLLEMR, is therefore a proper blending of HLL and HLLEM. As in the last cure [20], dissipation is gradually introduced into the basic scheme without using a partner auxiliary method. The resulting effects are very satisfactory, but the prescription is peculiar to the HLL family.

The analysis of the above remedies has been stimulating and led us to try to use a prescription for curing the carbuncle in FDSPAN, which can also be used in the FDS with the approximate solver of [15]. It is based on a detection routine, as in [20], but, in the present case, does not include the central element of the H-structure of interfaces. Let us consider, for instance, surface $(N, M+1/2)$ in Fig. 22. The first step of our cure consists in determining whether a "carbuncle-danger" exists for this interface or not, and if so, to what extent. To do this, we start to determine the maximum difference between the characteristic speeds across the four interfaces connected to $(N, M+1/2)$, which are indicated with crosses in Fig. 22. Such a maximum difference can be evaluated, considering, for instance, surface $(N+1/2, M)$, as

$$\epsilon_{N+1/2,M} = |\tilde{u}_{N+1,M} - \tilde{u}_{N,M}| + |a_{N+1,M} - a_{N,M}|, \tag{1}$$

where $\tilde{u}$ is the velocity component normal to the surface and a is the speed of sound. Then, the largest differences between the four computed ones is assigned to the interface

- **the two phases of the cure:**

1. **detection of the "dangerous regions"**

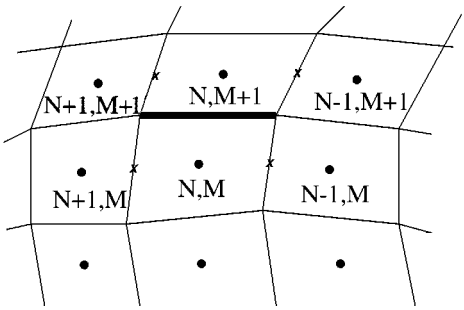

$$\epsilon_{N+1/2,M} = |\tilde{u}_{N+1,M} - \tilde{u}_{N,M}| + |a_{N+1,M} - a_{N,M}|$$

$$\eta_{N,M+1/2} = \max\{\epsilon_{N\pm1/2,M+K}\}_{K=0,1}$$

2. **injection of an appropriately tuned artificial dissipation**

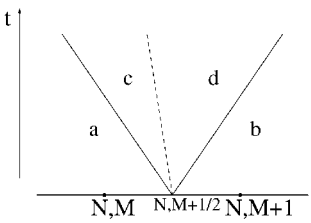

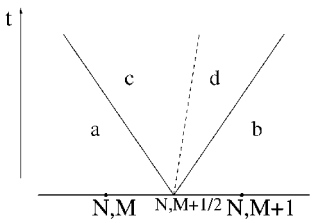

$$\mathcal{F}_{N,M+1/2} = \mathcal{F}_d - \eta_{N,M+1/2}\,(w_d - w_c)$$

$$\mathcal{F}_{N,M+1/2} = \mathcal{F}_c - \eta_{N,M+1/2}\,(w_d - w_c)$$

FIG. 22. The two steps of the cure.

$(N, M + 1/2)$ as a measure of the likelihood that a carbuncle may start there:

$$\eta_{N,M+1/2} = \max\{\epsilon_{N\pm1/2,M+K}\}_{K=0,1}. \tag{2}$$

In the following, $\eta_{N,M+1/2}$ is used to estimate the appropriate dissipation to be injected at the interface $(N, M + 1/2)$. It is important to notice that to avoid artificial viscosity from being erroneously injected in the presence of transverse density gradients, surface $N, M + 1/2$ itself was excluded from the characteristic speed difference evaluation.

Once η has been obtained, the RP is solved at $(N, M + 1/2)$. In the case of a moderate velocity of the contact surface and with the two acoustic waves traveling in opposite directions (see Fig. 22), two additional linear waves are imposed, one propagating leftward and the other rightward. These two waves present the same intensity, which is assumed to be equal to the product of η with the difference between the conservative variables across the contact surface. Thus, the global flux $\mathcal{F}$ across surface $N, M + 1/2$ is evaluated as

$$\mathcal{F}_{N,M+1/2} = \mathcal{F}_d - \eta_{N,M+1/2}(w_d - w_c) \tag{3}$$

or

$$\mathcal{F}_{N,M+1/2} = \mathcal{F}_c - \eta_{N,M+1/2}(w_d - w_c) \tag{4}$$

depending on whether the entropy wave is inclined leftward or rightward (Fig. 22).

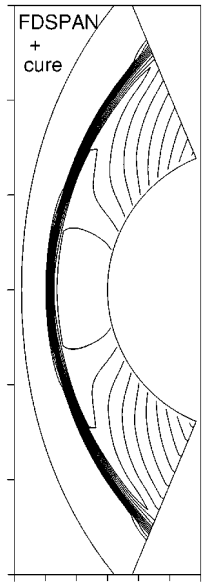

FIG. 23. Supersonic inviscid flow around a blunt body at $M_\infty = 20$ (density contours). FDSPAN with cure for the carbuncle.

Such a procedure can easily be interpreted as the translation of the *entropy fix* originally conceived for FDSROE (for the acoustic waves only) to the contact surface in FDSPAN. The cure is very efficient. The unacceptable blunt-body results of Fig. 6c become completely free of instabilities (Fig. 23) and, outside the shock-capturing zone, they are identical to the reference values of SHOFIT (Fig. 6m). The propagating shock, with the disturbing shape of Fig. 7c, becomes perfectly plane, without even the smallest perturbation. We consider the cure very attractive, because it is applied only where it is needed, that is, at the responsible interfaces inside the capturing zone of the shock. Moreover, it does not destroy the sharpness of density or shear velocity gradients, since the amount of the additional dissipation here becomes negligible.

7. CONCLUSIONS

In our work we show, through both numerical experiments and the linearized analyses of the algorithms, that the so-called carbuncle phenomenon affects those flux-difference splitting schemes that, when solving the Riemann Problem, explicitly take into account the presence of a contact surface.

The analysis of the linearized algorithms, originally proposed in [17] and extended here to a larger number of perturbations and to several different upwind methods, provides a useful tool to estimate, in advance, the occurrence of the numerical instability in any method only at the expense of some algebra and without the necessity of implementing the method in a code. In addition, such an analysis helps us to understand the approach of different upwind schemes to the Riemann problem and to appreciate how close (or far) they are from the correct method of characteristics.

The cure that we propose as a remedy to the carbuncle effects appears to be effective and efficient; it automatically introduces artificial dissipation only in those localized regions

where some control of the carbuncle instability is required, but it does not act in the remaining flow-field, where the numerical viscosity is only related to the basic scheme used.

APPENDIX A

How to Obtain the Formulas Presented in Table I

Here we show how the value of the flux at the interface reported in Table I ($\mathbf{G}_{M+\frac{1}{2}} = (G_1, G_2, G_3, G_4)^T_{M+\frac{1}{2}}$) can be obtained for some of the upwind methods considered, in particular for MOC, FDSROE, FDSPAN, FVSVL, HLL, AUSM-VEL, AUSM-M, and AUSM+. We refer to the problem described in Section 5 and to the relative definitions given there. The flow is governed by the Euler equations for a perfect gas. Since we suppose the flow to be uniform along x with any variation only occurring along y, we hereafter drop, in this Appendix, the index N, which denotes a computational location, so that the identification N, M will be reduced to M. We assume initial values at cells (M) and $(M+1)$:

$$\begin{aligned} \rho_M &= 1+\hat{\rho}, & \rho_{M+1} &= 1-\hat{\rho}, \\ u_M &= u_0+\hat{u}, & u_{M+1} &= u_0-\hat{u}, \\ v_M &= 0, & v_{M+1} &= 0, \\ p_M &= 1+\hat{p}, & p_{M+1} &= 1-\hat{p}. \end{aligned} \tag{5}$$

Since perturbations $\hat{\rho}$, $\hat{u}$, and $\hat{p}$ are small, one obtains

$$a_M = \sqrt{\gamma}\left(1+\frac{\hat{p}}{2}-\frac{\hat{\rho}}{2}\right), \quad a_{M+1} = \sqrt{\gamma}\left(1-\frac{\hat{p}}{2}+\frac{\hat{\rho}}{2}\right), \tag{6}$$

where γ is the ratio of the specific heats ($\gamma = 1.4$).

The conservative variables $\mathbf{W} = (\rho, \rho u, \rho v, e)^T$ and the components of the flux $\mathbf{G} = (\rho v, \rho uv, p+\rho v^2, v(p+e))^T$ associated with the y -direction, at cells (M) and $(M+1)$, are

$$\mathbf{W}_M = \begin{vmatrix} 1+\hat{\rho} \\ u_0\left(1+\hat{\rho}+\frac{\hat{u}}{u_0}\right) \\ 0 \\ \frac{1+\hat{p}}{\gamma-1}+\frac{u_0^2}{2}\left(1+\hat{\rho}+2\frac{\hat{u}}{u_0}\right) \end{vmatrix}; \qquad \mathbf{W}_{M+1} = \begin{vmatrix} 1-\hat{\rho} \\ u_0\left(1-\hat{\rho}-\frac{\hat{u}}{u_0}\right) \\ 0 \\ \frac{1-\hat{p}}{\gamma-1}+\frac{u_0^2}{2}\left(1-\hat{\rho}-2\frac{\hat{u}}{u_0}\right) \end{vmatrix} \tag{7}$$

and

$$\mathbf{G}_M = \begin{vmatrix} 0 \\ 0 \\ 1 \\ 0 \end{vmatrix}; \quad \mathbf{G}_{M+1} = \begin{vmatrix} 0 \\ 0 \\ 1 \\ 0 \end{vmatrix}. \tag{8}$$

On the basis of these initial data, we estimate flux $\mathbf{G}_{M+\frac{1}{2}}$ at the interface $(M+\frac{1}{2})$.

MOC, FDSROE, and FDSPAN

The solution of the RP according to the MOC is based upon the conservation of the signals $R_{1,3} = p \mp \sqrt{\gamma} v$, $R_2 = \frac{p}{\rho^\gamma}$, and $R_4 = u$ along the corresponding characteristic rays. The flow properties at interface $(M + \frac{1}{2})$ are evaluated from these conditions:

$$p_{M+\frac{1}{2}} + \sqrt{\gamma} v_{M+\frac{1}{2}} = p_M + \sqrt{\gamma} v_M, \tag{9a}$$

$$p_{M+\frac{1}{2}} - \sqrt{\gamma} v_{M+\frac{1}{2}} = p_{M+1} - \sqrt{\gamma} v_{M+1}, \tag{9b}$$

$$p_{M+\frac{1}{2}}/\rho^\gamma_{M+\frac{1}{2}} = \begin{cases} p_M/\rho^\gamma_M & \text{if } \hat{p} > 0, \\ p_{M+1}/\rho^\gamma_{M+1} & \text{otherwise,} \end{cases} \tag{9c}$$

$$u_{M+\frac{1}{2}} = \begin{cases} u_M & \text{if } \hat{p} > 0, \\ u_{M+1} & \text{otherwise.} \end{cases} \tag{9d}$$

From Eqs. (5), we obtain

$$\rho_{M+\frac{1}{2}} = \begin{cases} 1 + \hat{\rho} - \frac{\hat{p}}{\gamma} & \text{if } \hat{p} > 0, \\ 1 - \hat{\rho} + \frac{\hat{p}}{\gamma} & \text{otherwise,} \end{cases} \tag{10a}$$

$$u_{M+\frac{1}{2}} = \begin{cases} u_0 + \hat{u} & \text{if } \hat{p} > 0, \\ u_0 - \hat{u} & \text{otherwise,} \end{cases} \tag{10b}$$

$$v_{M+\frac{1}{2}} = \frac{\hat{p}}{\sqrt{\gamma}}, \tag{10c}$$

$$p_{M+\frac{1}{2}} = 1. \tag{10d}$$

Finally, the resulting flux $\mathbf{G}_{M+\frac{1}{2}}$ is

$$\mathbf{G}_{M+\frac{1}{2}} = \begin{vmatrix} \frac{\hat{p}}{\sqrt{\gamma}} \\ u_0 \frac{\hat{p}}{\sqrt{\gamma}} \\ 1 \\ \left(\frac{\gamma}{\gamma-1} + \frac{u_0^2}{2}\right)\frac{\hat{p}}{\sqrt{\gamma}} \end{vmatrix}. \tag{11}$$

This estimate corresponds to the exact solution of the RP because the perturbations $(\hat{\rho}, \hat{u}, \hat{p})$ are small and no intense shock waves are expected. The solution is also the same for FDSROE (since the approximate solver proposed in [19] becomes exact if small initial discontinuities define the RP) and for FDSPAN [16] and for the method proposed in [15] (because the only approximation in these two solvers is introduced in the case of intense shock waves).

FVSVL

In the FVSVL method [24], the following local splitting of the flux is defined:

$$\mathbf{G}^\pm = \pm\frac{\rho}{4a}(v \pm a)^2 \begin{vmatrix} 1 \\ u \\ (\gamma-1)v \pm 2a \\ \frac{((\gamma-1)v \pm 2a)^2}{2(\gamma^2-1)} + \frac{u^2}{2} \end{vmatrix}. \tag{12}$$

The interface flux $\mathbf{G}_{M+\frac{1}{2}}$ is given by

$$\mathbf{G}_{M+\frac{1}{2}} = \mathbf{G}^{+}_{M} + \mathbf{G}^{-}_{M+1}, \tag{13}$$

which, on the basis of the assumed initial values, becomes

$$\mathbf{G}_{M+\frac{1}{2}} = \begin{vmatrix} \frac{\sqrt{\gamma}}{4}(\hat{p}+\hat{\rho}) \\ u_0\frac{\sqrt{\gamma}}{4}\left(\hat{p}+\hat{\rho}+2\frac{\hat{u}}{u_0}\right) \\ 1 \\ \frac{\sqrt{\gamma}\gamma}{2(\gamma^2-1)}(3\hat{p}-\hat{\rho})+u_0^2\frac{\sqrt{\gamma}}{8}\left(\hat{p}+\hat{\rho}+4\frac{\hat{u}}{u_0}\right) \end{vmatrix}. \tag{14}$$

The interface flux for FVSSW [21] is evaluated in a very similar manner.

HLL

In the HLL method [6], the flux at the interface is estimated as

$$\mathbf{G}_{M+\frac{1}{2}} = \frac{\lambda_R\mathbf{G}_M - \lambda_L\mathbf{G}_{M+1}}{\lambda_R-\lambda_L} + \frac{\lambda_R\lambda_L}{\lambda_R-\lambda_L}(\mathbf{W}_{M+1}-\mathbf{W}_M) \tag{15}$$

where, as reported in [6], "λ_L and λ_R are the lower and upper bounds, respectively, for the smallest and largest signal velocity, calculated according to some algorithm." Using Eqs. (7) and (8), we obtain

$$\mathbf{G}_{M+\frac{1}{2}} = \begin{vmatrix} \sqrt{\gamma}\hat{\rho} \\ u_0\sqrt{\gamma}\left(\hat{\rho}+\frac{\hat{u}}{u_0}\right) \\ 1 \\ \frac{\sqrt{\gamma}}{\gamma-1}\hat{p}+u_0^2\frac{\sqrt{\gamma}}{2}\hat{\rho}+u_0^2\sqrt{\gamma}\frac{\hat{u}}{u_0} \end{vmatrix}. \tag{16}$$

AUSM-VEL

Looking at the method AUSM-VEL and the relative definitions given in [11], we obtain for the convective terms

$$v^{+}_{M} = \frac{a_M}{4}, \qquad v^{-}_{M+1} = -\frac{a_{M+1}}{4} \tag{17}$$

and for the pressure splitting

$$p^{+}_{M} = \frac{p_M}{2}, \qquad p^{-}_{M+1} = \frac{p_{M+1}}{2}. \tag{18}$$

Therefore, following [11], we have

$$v_{M+\frac{1}{2}} = v^{+}_{M} + v^{-}_{M+1} = \frac{\sqrt{\gamma}}{4}(\hat{p}-\hat{\rho}), \tag{19a}$$

$$p_{M+\frac{1}{2}} = p^{+}_{M} + p^{-}_{M+1} = 1, \tag{19b}$$

and

$$\Phi_M = \begin{vmatrix} 1+\hat{\rho} \\ u_0\left(1+\hat{\rho}+\frac{\hat{u}}{u_0}\right) \\ 0 \\ \frac{\gamma}{\gamma-1}(1+\hat{p})+\frac{u_0^2}{2}\left(1+\hat{\rho}+2\frac{\hat{u}}{u_0}\right) \end{vmatrix};$$
$$\Phi_{M+1} = \begin{vmatrix} 1-\hat{\rho} \\ u_0\left(1-\hat{\rho}-\frac{\hat{u}}{u_0}\right) \\ 0 \\ \frac{\gamma}{\gamma-1}(1-\hat{p})+\frac{u_0^2}{2}\left(1-\hat{\rho}-2\frac{\hat{u}}{u_0}\right) \end{vmatrix}. \tag{20}$$

The interface flux is defined as

$$\mathbf{G}_{M+\frac{1}{2}} = \begin{cases} v_{M+\frac{1}{2}}\Phi_M & \text{if } v_{M+\frac{1}{2}} > 0, \\ v_{M+\frac{1}{2}}\Phi_{M+1} & \text{otherwise} \end{cases} + \begin{vmatrix} 0 \\ 0 \\ p_{M+\frac{1}{2}} \\ 0 \end{vmatrix}. \tag{21}$$

It therefore follows that

$$\mathbf{G}_{M+\frac{1}{2}} = \begin{vmatrix} \frac{\sqrt{\gamma}}{4}(\hat{p}-\hat{\rho}) \\ u_0\frac{\sqrt{\gamma}}{4}(\hat{p}-\hat{\rho}) \\ 1 \\ \left(\frac{\gamma}{\gamma-1}+\frac{u_0^2}{2}\right)\frac{\sqrt{\gamma}}{4}(\hat{p}-\hat{\rho}) \end{vmatrix}. \tag{22}$$

AUSM-M

The AUSM-M method is described in [12]. On the basis of the definitions given there, we obtain

$$M_M^+ = \frac{1}{4}, \qquad M_{M+1}^- = -\frac{1}{4}, \tag{23a}$$
$$p_M^+ = \frac{p_M}{2}, \qquad p_{M+1}^- = \frac{p_{M+1}}{2}. \tag{23b}$$

Therefore,

$$M_{M+\frac{1}{2}} = M_M^+ + M_{M+1}^- = 0, \tag{24a}$$
$$p_{M+\frac{1}{2}} = p_M^+ + p_{M+1}^- = 1. \tag{24b}$$

With the previous definitions of Φ_M and Φ_{M+1}, the interface flux is defined as

$$\mathbf{G}_{M+\frac{1}{2}} = \begin{cases} M_{M+\frac{1}{2}}a_M\Phi_M & \text{if } v_{M+\frac{1}{2}} > 0, \\ M_{M+\frac{1}{2}}a_{M+1}\Phi_{M+1} & \text{otherwise} \end{cases} + \begin{vmatrix} 0 \\ 0 \\ p_{M+\frac{1}{2}} \\ 0 \end{vmatrix}. \tag{25}$$

Since $M_{M+\frac{1}{2}} = 0$, we have

$$\mathbf{G}_{M+\frac{1}{2}} = \begin{vmatrix} 0 \\ 0 \\ 1 \\ 0 \end{vmatrix} \tag{26}$$

as reported in Table I.

AUSM+

The most recent AUSM+ method is described in [13]. With the definitions given there and the usual initial values, we have

$$\mathcal{M}_\beta^+ = \frac{1}{4} + \beta, \quad \mathcal{M}_\beta^- = -\frac{1}{4} - \beta, \tag{27a}$$

$$\mathcal{P}_\alpha^+ = \frac{1}{2}, \qquad \mathcal{P}_\alpha^- = \frac{1}{2}, \tag{27b}$$

It therefore follows that

$$m_{M+\frac{1}{2}} = \mathcal{M}_\beta^+ + \mathcal{M}_\beta^- = 0, \tag{28a}$$

$$p_{M+\frac{1}{2}} = \mathcal{P}_\alpha^+ p_M + \mathcal{P}_\alpha^- p_{M+1} = 1. \tag{28b}$$

Furthermore, a value of the interface speed of sound $a_{M+\frac{1}{2}}$ is somehow determined in [13] and the interface flux is defined as

$$\mathbf{G}_{M+\frac{1}{2}} = \begin{cases} m_{M+\frac{1}{2}} a_{M+\frac{1}{2}} \Phi_M & \text{if } m_{M+\frac{1}{2}} > 0, \\ m_{M+\frac{1}{2}} a_{M+\frac{1}{2}} \Phi_{M+1} & \text{otherwise} \end{cases} + \begin{vmatrix} 0 \\ 0 \\ p_{M+\frac{1}{2}} \\ 0 \end{vmatrix}. \tag{28}$$

Since $m_{M+\frac{1}{2}} = 0$, we have, as in the previous method,

$$\mathbf{G}_{M+\frac{1}{2}} = \begin{vmatrix} 0 \\ 0 \\ 1 \\ 0 \end{vmatrix}. \tag{29}$$

The values of the components $(G_1)_{M+\frac{1}{2}}$, $(G_2)_{M+\frac{1}{2}}$, $(G_3)_{M+\frac{1}{2}}$, and $(G_4)_{M+\frac{1}{2}}$ of the flux $\mathbf{G}_{M+\frac{1}{2}}$ estimated in Eqs. (11), (14), (16), (22), (26), and (29) are reported in Table I.

APPENDIX B

How to Obtain the Formulas Presented in Table II

We use the evaluations of the interface flux reported in Table I to obtain the recursive formulas shown in Table II. As in the previous Appendix A, we here drop the index N to

denote a computational location. We assume the initial data at the step K given by

$$\rho^K = 1 \pm \hat{\rho}^K, \tag{30a}$$

$$u^K = u_0 \pm \hat{u}^K, \tag{30b}$$

$$v^K = 0, \tag{30c}$$

$$p^K = 1 \pm \hat{p}^K, \tag{30d}$$

where the $+$ sign refers to the cell (M) and the $-$ sign to the neighboring cells $(M-1)$ and $(M+1)$. Starting from step K, we integrate, in time, the governing laws of conservation at the cell (M), on the basis of the plain first-order scheme. The result at step $K+1$ is represented by

$$\mathbf{W}_M^{K+1} = \mathbf{W}_M^K - \frac{\nu}{|v|+a}\left(\mathbf{G}_{M+\frac{1}{2}}^K - \mathbf{G}_{M-\frac{1}{2}}^K\right), \tag{31}$$

where ν is the Courant number. It is convenient to introduce the perturbations of the conservative variable at cell (M) and of the flux at interface $(M+\frac{1}{2})$,

$$\hat{\mathbf{W}}_M = \begin{vmatrix} \hat{\rho} \\ u_0\left(\hat{\rho} + \frac{\hat{u}}{u_0}\right) \\ 0 \\ \frac{\hat{p}}{\gamma-1} + u_0^2 2\left(\hat{\rho} + 2\frac{\hat{u}}{u_0}\right) \end{vmatrix}, \tag{31a}$$

$$\hat{\mathbf{G}}_{M+\frac{1}{2}} = \mathbf{G}_{M+\frac{1}{2}} - \begin{vmatrix} 0 \\ 0 \\ 1 \\ 0 \end{vmatrix}, \tag{31b}$$

where $\mathbf{G}_{M+\frac{1}{2}}$ is given in Table I. Since the flow properties at cells $(M-1)$ and $(M+1)$ are the same, the difference of the flux at interfaces $(M+\frac{1}{2})$ and $(M-\frac{1}{2})$ is given by

$$\mathbf{G}_{M+\frac{1}{2}}^K - \mathbf{G}_{M-\frac{1}{2}}^K = 2\hat{\mathbf{G}}_{M+\frac{1}{2}}. \tag{32}$$

Moreover, the characteristic slope $(|v|+a)$ tends to $\sqrt{\gamma}$. Therefore, the integration scheme (Eq. 31) gives

$$\hat{\mathbf{W}}_M^{K+1} = \hat{\mathbf{W}}_M^K - \frac{2\nu}{\sqrt{\gamma}}\hat{\mathbf{G}}_{M+\frac{1}{2}}^K. \tag{33}$$

We define $(\hat{G}_i)_{M+\frac{1}{2}}^K$ as being the i component of vector $\hat{\mathbf{G}}_{M+\frac{1}{2}}^K$. Then, from Eq. (33), the integration of the first law of conservation (continuity) gives

$$\hat{\rho}_M^{K+1} = \hat{\rho}_M^K - \frac{2\nu}{\sqrt{\gamma}}(\hat{G}_1)_{M+\frac{1}{2}}^K. \tag{34}$$

The integration of the second law of conservation (x-momentum) and the above Eq. (34) yields

$$\hat{u}_M^{K+1} = \hat{u}_M^K - \frac{2\nu}{\sqrt{\gamma}}\left(-u_0(\hat{G}_1)^K_{M+\frac{1}{2}} + (\hat{G}_2)^K_{M+\frac{1}{2}}\right). \tag{35}$$

The integration of the third conservation law (y-momentum) leads to

$$\hat{v}_M^{K+1} = \hat{v}_M^K - \frac{2\nu}{\sqrt{\gamma}}(\hat{G}_3)^K_{M+\frac{1}{2}}. \tag{36}$$

The integration of the fourth law of conservation (energy) and Eqs. (34)–(36) give

$$\hat{p}_M^{K+1} = \hat{p}_M^K - \frac{2\nu}{\sqrt{\gamma}}(\gamma-1)\left(\frac{u_0^2}{2}(\hat{G}_1)^K_{M+\frac{1}{2}} - u_0(\hat{G}_2)^K_{M+\frac{1}{2}} + (\hat{G}_4)^K_{M+\frac{1}{2}}\right). \tag{37}$$

By taking the value of the components $(\hat{G}_1)^K_{M+\frac{1}{2}}$, $(\hat{G}_2)^K_{M+\frac{1}{2}}$, $(\hat{G}_3)^K_{M+\frac{1}{2}}$, and $(\hat{G}_4)^K_{M+\frac{1}{2}}$ of $\hat{\mathbf{G}}^K_{M+\frac{1}{2}}$ that can be obtained from Table I for each method, we obtain the recursive formulas of Table II.

REFERENCES

1. P. Charrier, B. Dubrocca, and L. Flandrin, An approximate Riemann solver of hypersonic bidimensional flows, *C. R. Acad. Sci. Paris* Ser. 1 **317**, 1083 (1993).
2. F. Coquel and M. S. Liou, Field by field hybrid upwind splitting methods, AIAA Paper 93-3302-CP (1993).
3. B. Einfeldt, On Godunov-type methods for gas dynamics, *SIAM J. Numer. Anal.* **25**(2), 294 (1988).
4. B. Einfeldt, C. D. Munz, P. L. Roe, and B. Sjögreen, On Godunov-type methods near low density, *J. Comput. Phys.* **92**, 273 (1991).
5. S. K. Godunov, A finite-difference method for the numerical computation of discontinuous solutions of the equations of fluid dynamics, *Mat. Sb.* **47**, 271 (1959).
6. A. Harten, P. D. Lax, and B. Van Leer, On upstream and Godunov-type schemes for hyperbolic conservation laws, *SIAM Rev.* **25**(1), 35 (1983).
7. D. Hänel, R. Schwane, and G. Seider, On the accuracy of upwind schemes for the solution of the Navier-Stokes equations, AIAA Paper 87-1105, in *Proc. AIAA 8th Computational Fluid Dynamics Conference, 1987*, pp. 42–46.
8. A. Harten and J. M. Hymax, Self adjusting grid methods for one-dimensional hyperbolic conservation laws, *J. Comput. Phys.* **50**, 235 (1983).
9. K. H. Kim, J. H. Lee, and O. H. Rho, An improvement of AUSM schemes by introducing the pressure-based weight functions, *Comput. Fluids* **27**(3), 311 (1998).
10. J. J. Korte, *An Explicit Upwind Algorithm for Solving the Parabolized Navier-Stokes Equations*, Technical Paper 3050 (NASA, February, 1991).
11. M. S. Liou, *On a New Class of Flux Splitting*, Lecture Notes in Physics (Springer-Verlag, Berlin, 1993), Vol. 414.
12. M. S. Liou and C. J. Steffen, A new flux splitting scheme, *J. Comput. Phys.* **107**, 23 (1993).
13. M. S. Liou, A sequel to AUSM: AUSM+, *J. Comput. Phys.* **129**, 364 (1996).
14. M. S. Liou, Probing numerical fluxes: Mass flux, positivity and entropy-satisfying property, AIAA Paper 97-2035 (1997).
15. S. Osher and F. Solomon, Upwind schemes for hyperbolic systems of conservation laws, *Math. Comput.* **38**, 339 (1982).
16. M. Pandolfi, A contribution to the numerical prediction of unsteady flows, *AIAA J.* **22**, 602 (1984).

17. J. J. Quirk, *A Contribution to the Great Riemann Solver Debate*, ICASE Report 92-64 (1992).
18. R. Radespiel and N. Kroll, Accurate flux vector splitting for shocks and shear layers, *J. Comput. Phys.* **121**, 66 (1991).
19. P. L. Roe, Approximate Riemann solvers, parameter vectors and difference schemes, *J. Comput. Phys.* **43**, 357 (1981).
20. R. Sanders, E. Morano, and M.-C. Druguet, Multidimensional dissipation for upwind schemes: Stability and applications to gas dynamics, *J. Comput. Phys.* **145**, 511 (1998).
21. J. L. Steger and R. F. Warming, Flux splitting of the inviscid gasdynamic equations with application to finite-difference methods, *J. Comput. Phys.* **40**, 263 (1981).
22. E. F. Toro, M. Spruce, and W. Speares, Restoration of the contact surface in the HLL-Riemann solver, *Shock Waves* **4**, 25 (1994).
23. J. van Keuk, J. Ballmann, A. Schneider, and W. Koschel, Numerical simulation of hypersonic inlet flows, in *Proc. of the AIAA 8th International Space Plane and Hypersonic Systems and Technologies Conference, Norfolk VA, 1998*.
24. B. Van Leer, *Flux-Vector Splitting for the Euler Equations* Lectures Notes in Physics (Springer-Verlag, Berlin, 1982), Vol. 170.
25. Y. Wada and M. S. Liou, *A Flux Splitting Scheme with High-Resolution and Robustness for Discontinuities*, NASA T. M. 106452 (1994).
26. Y. Wada and M. S. Liou, An accurate and robust flux splitting scheme for shock and contact discontinuities, *SIAM J. Sci. Comput.* **18**(3), 633 (1997).
27. R. Walder, *Some Aspects of the Computational Dynamics of Colliding Flows in Astrophysical Nebulae*, Diss. ETH No. 10302 (ETH, Zürich, 1993).